Supplement of Hydrol. Earth Syst. Sci., 20, 411–430, 2016
http://www.hydrol-earth-syst-sci.net/20/411/2016/
doi:10.5194/hess-20-411-2016-supplement

Hydrology and Earth System Sciences
Open Access

Supplement of

Spatio-temporal variability of snow water equivalent in the extra-tropical Andes Cordillera from distributed energy balance modeling and remotely sensed snow cover

E. Cornwell et al.

Correspondence to: J. McPhee (jmcphee@u.uchile.cl)

- hess-20-411-2016-supplement-title-page.pdf
- Supplement.docx

Spatio-temporal variability of snow water equivalent in the extra-tropical Andes Cordillera from distributed energy balance modeling and remotely sensed snow cover

S1 Definition of homogenous regions

Figure S1 shows the outcome of the clustering process based on spring and summer (September to March) season total river flow volume (SSRV). The procedure consists on grouping catchments in the Andes cordillera between 27 ° S and 38 ° S and calculating the SSRV (natural regime) for each one, performing a clustering procedure using an algorithm for variance minimization (Rubio-Álvares y McPhee, 2010; Wilks, 2005**).** SSRV values are computed for 2001 – 2014, seeking minimum data loss for this purpose (Sawicz et al., 2011). After defining a consistency threshold for both Andes slopes - by identifying an abrupt slope change in the cumulative distance / algorithm-step curve - a total of eight clusters are defined: three (C1, C2 and C3) on the western slope and five (C4 through C8) on the eastern slope of the Andes range. The northern clusters (C1 and C4) correspond to arid to semi-arid climates, whereas C2, C5 and C6 are characterized predominantly by Mediterranean conditions. C3, C7 and C8 include basins in the southern domain, where the Andes display a lower elevation and where liquid precipitation inputs during the winter and spring seasons are more frequent. Note that each cluster contains only adjacent basins which highlights the hydro-climatic character of this classification.

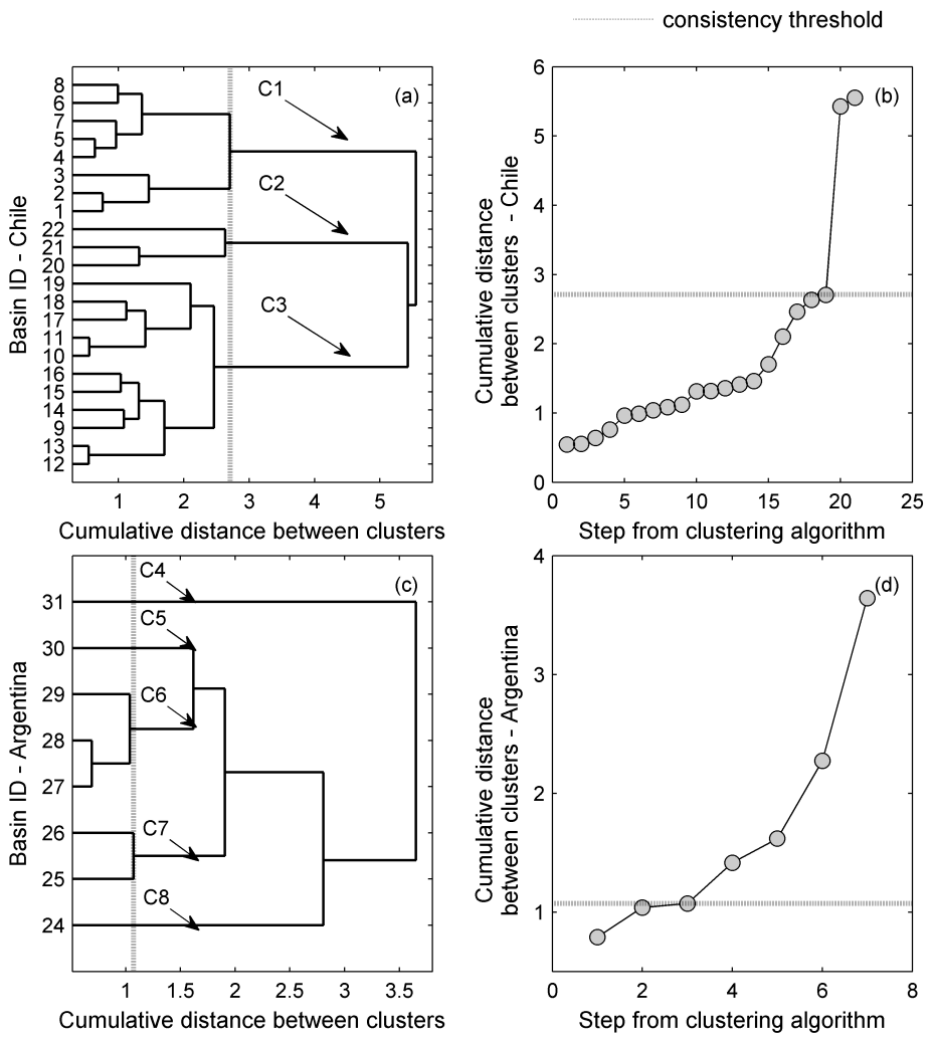

Figure S1. Clusterization process and outcomes for both eastern and western central Andes sides.

Figure S2 shows the elevation distribution within each cluster, and illustrates the elevation of the available meteorological stations for forcing data extrapolation. It is apparent that station locations on the western slope of the domain (clusters C1, C2 and C3) are more representative of average cluster conditions under the assumption that elevation plays a major role in controlling each cluster's climate. Eastern slope (Clusters C4 through C8) stations are located at lower elevations, which may impact the spatial extrapolation of model parameters as discussed in the main manuscript.

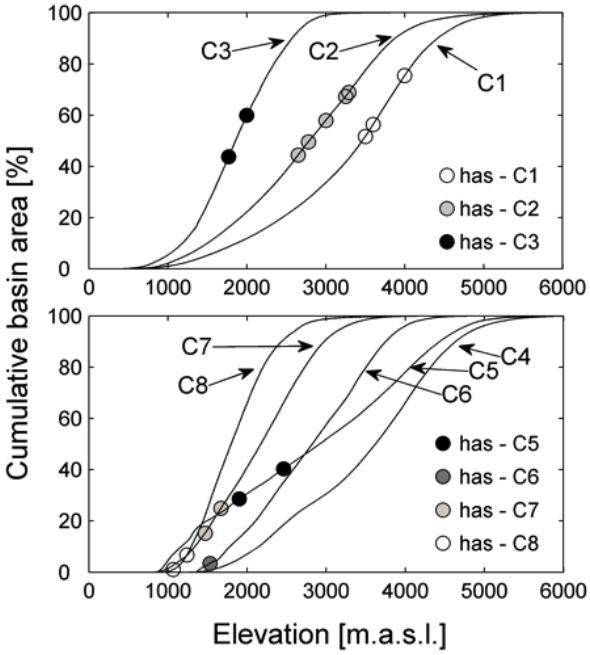

Figure S2. Hypsometric curves of clusters in the model domain, and approximate elevation of meteorological stations.

S2 Air temperature spatial distribution

Figure S3 illustrates the linear correlation between air temperature differences among pairs of high elevation and valley meteorological stations and the corresponding land surface temperature differences between matching pixels in the MODIS LST product. A consequence of the strong linear relation is that it is possible to extrapolate air temperature differences across model pixels based on the spatial distribution of remotely sensed surface temperatures.

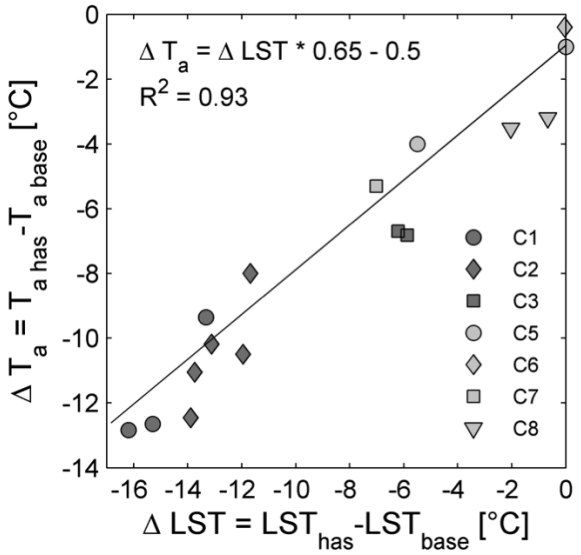

Figure S3. Linear regression between MODIS LST and index station observed air temperature. Symbols refer to each modeling cluster, C1 - C3 are cluster on the western slope, C4 - C8 are clusters on the eastern slope of the mountain range.

S3 Timing peak SWE for eastern and western slopes of the central Andes range

Peak SWE timing estimation is carried out to in order to define a specific date for modeled SWE comparison with snow pillow data and river flow. Figure S4a shows timing peak SWE frequency between 15Aug - 15 Sep for stations on the western side of the continental divide. For eastern slope locations, peak SWE shifts into 15 Sep - 15 Oct. Notwithstanding elevation controls, a general behavior could be observed by averaging snow pillows time series fortnightly. A generalized peak SWE date could be assumed from Figure S4b as follows: for the western side we adopted September first as date for peak SWE (MSWE) validation; whereas for the eastern slope we assume October first. Note that in the case of snow surveys we considered the exact date of the field campaign. The literature reports similar behavior for MSWE (Masiokas et al., 2006), showing variable timing MSWE frequency for several snow pillows located at C2, C3 and C5 clusters.

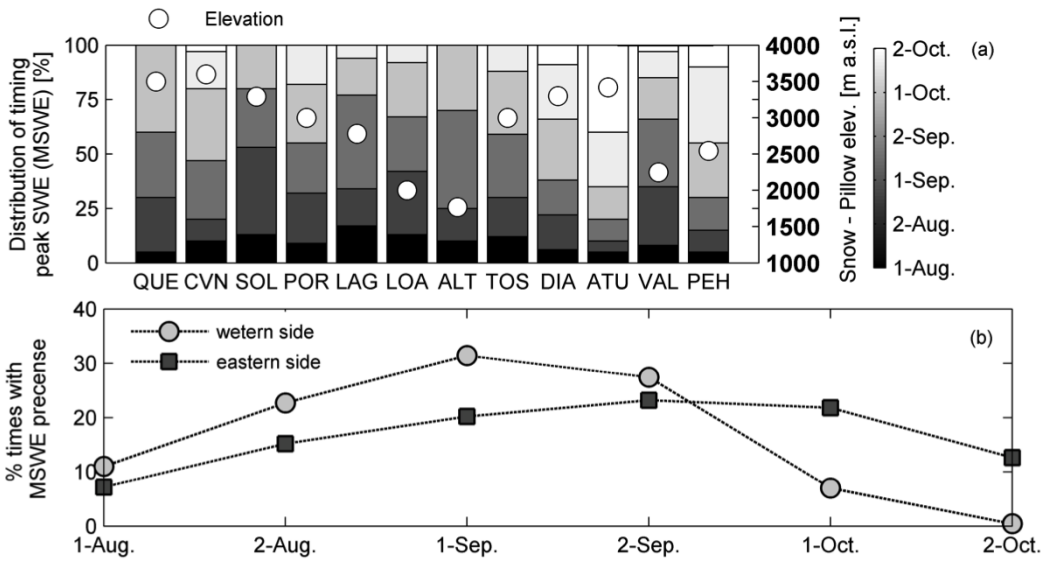

Figure S4. Average timing peak SWE for eastern and western cordillera.

S4 fSCA cloud cover post-processing

A post-processing algorithm was applied over raw MOD10A1 fractional snow cover area (fSCA) satellite product (and also to MOD11A1 Land Surface Temperature) in order to minimize the effect generated by cloud cover and missing pixel values. The algorithm used in this work is an adaptation from Gafurov and Bárdossy (2009), extended for fractional values. Given a pixel *p(x y,t, r)*, where *x* = latitude position, *y* = longitude position, *t* = day and *y* = year; the first step (s1) includes temporal interpolation pixel fill for consecutively ± 1, 2 and 3 days over valid pixels:

$$p(x,y,t,r)^{s1} = \left(\frac{p(x,y,t+n,r) - p(x,y,t-m,r)}{|n+m|}\right)|t-m| + p(x,y,t-m,r) \quad \textbf{[1]}$$

$$\text{with } 1 \leq n,m \leq 3$$

Values of *n* and *m* are chosen in order to minimize $|n+m|$. The second step (s2) includes a spatial kernel-average pixel filling with *x* ± 1, *y* ±1 setting considering only those valid pixels with lower elevation $z = (x,y)$ than the central pixel:

$$p(x,y,t,r)^{s2} = \sum_{i=-1}^{i=1} \sum_{i=-j}^{i=j} \frac{1}{k} p(i,j,t,r)_{i \neq j}{}^{s1}$$

$$\text{where } k = \begin{cases} 1 \; if \; z(x,y)_{x \neq y} \leq z(x,y) \\ 0 \quad \text{otherwise} \end{cases} \qquad \textbf{[2]}$$

The third step includes filling with the average value over the 2001- 2014 period over valid pixels if steps 1 and 2 are infeasible. This step ensures the absence of null pixels:

$$p(x,y,t,r)^{s3} = \sum_{r=2001}^{r=2014} \frac{1}{k} p(x,y,t,r)^{s2} \;\; , \;\; \text{where } k = \begin{cases} 1 \text{ for null values} \\ 0 \text{ otherwise} \end{cases} \qquad \textbf{[3]}$$

For MOD11A1 Land Surface Temperature, algorithm uses (1) temporal interpolation pixel fill considering 2 days prior and posterior to the estimated day. Subsequently, MOD11A1 post-processing algorithm uses an alternative step 2 based on skin temperature – elevation linear correlation (Colombi, 2007) over $p(x,y,t,r)^{s1}$ null pixels:

$$p(x,y,t,r)^{s2} = a\, z(x,y) + b \qquad \textbf{[4]}$$

The outcomes from fSCA post-processing are shown in Figure S5. Cluster 3 (C3) and cluster 4 (C4) represent most wet (southern) and dry (northern) zones in the spatial domain. The dots represent raw data and the continuous line represents post-processed time series from a spatial average estimation. Cloudy conditions in C3 impose significant uncertainty between August and November. Post-processed fSCA seems to alleviate this problem (15% or lower cloud cover area) especially in 2005, 06, 08, 09, 10, 11 and 12 for peak and lower values. C3 maximum fSCA reaches 70% – 90% unlike C4, where fSCA reaches up to 25% - 50%. In this zone, cloud cover introduces less uncertainty than C3, showing good agreement with raw data (also for 15% or lower cloud cover area) almost every year. Temporal dynamics from fSCA reveals partial SCA decay interrupted by occasional spring snowfall events and high frequency noise.

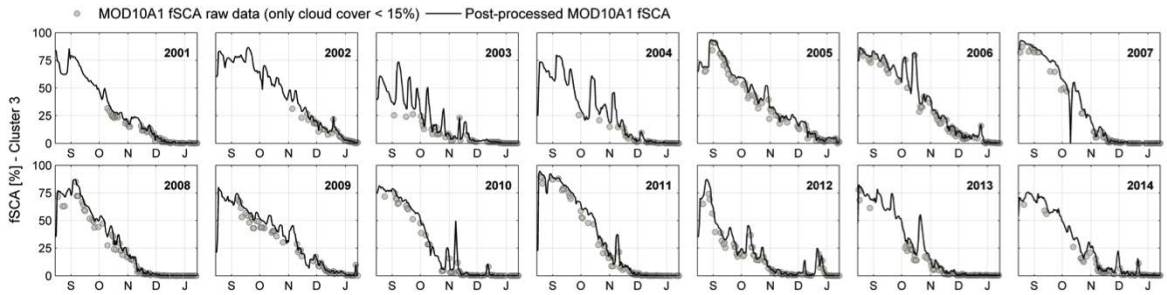

Figure S5a. Cloud cover post-processing for cluster 3 – southern Chile fSCA (spatial average).

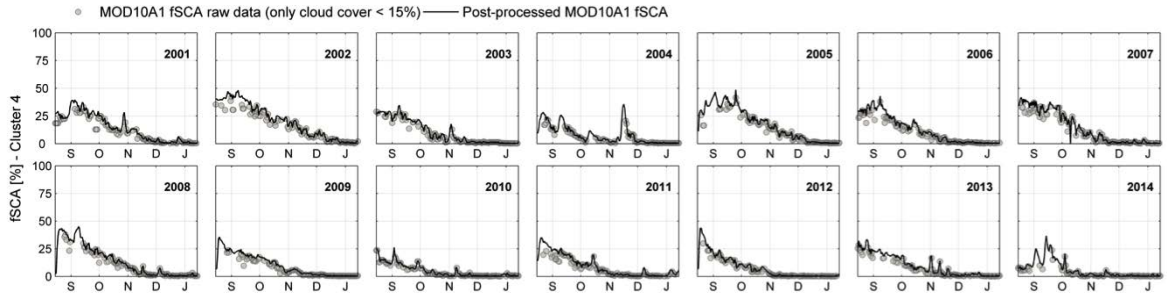

Figure S5b. Cloud cover post-processing for cluster 4 – northern Argentina fSCA (spatial average).

S5 Turbulent energy flux analysis at meteorological stations

In order to diagnose differential performance of the model across the hydrologic units defined in this study, we estimate latent and sensible heat fluxes at point scale from data available only at the few high elevation meteorological stations in the region (with recorded relative humidity). Our analysis confirms that for the stations located within cluster C1, latent heat fluxes have opposite sign and dominate over sensible heat fluxes (Figure S6), which results in net turbulent cooling of the snowpack. On the other hand, data from stations located on the eastern side of the continental divide show positive latent heat fluxes, indicating predominance of condensation over sublimation at those sites.

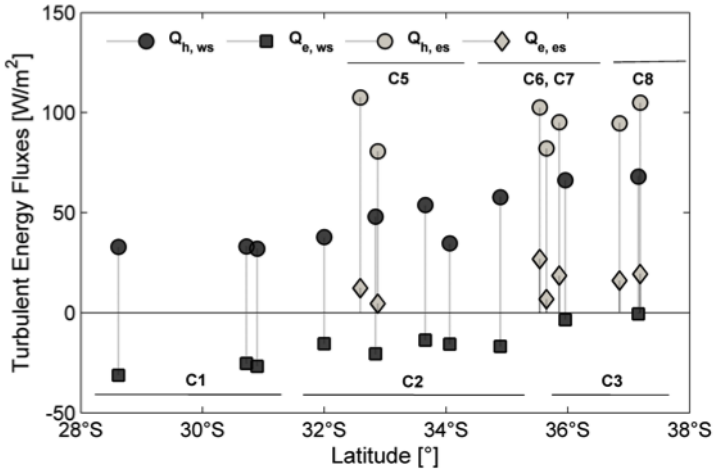

Figure S6. Computed from meteorological records at index stations associated with each basin cluster.

S6 Modeled SWE decay and spatial patterns

Figure S7 presents a time series evaluation of reconstructed SWE at two snow pillow sites. Portillo (POR) shows the worst model skill in terms of R^2 with a value of 0.32, whereas Lo Aguirre (LOA) shows the best performance with a value of R^2 of 0.88. The series compared are simply the observation at the snow pillow instrument versus the closest pixel-wide value obtained from the reconstruction, with no downscaling attempted. Comparisons between point-scale and pixel-scale variables are always problematic, and in the case of SWE this is specially true given the high spatial variability to be expected at lengths higher that a few tens of meters. In areas of abrupt topography, as is the case of the model domain, the discrepancies may increase because even small offsets in the grid position can result in areas of preferential accumulation being over- or under-represented, thus introducing a systematic bias in the estimation from fSCA.

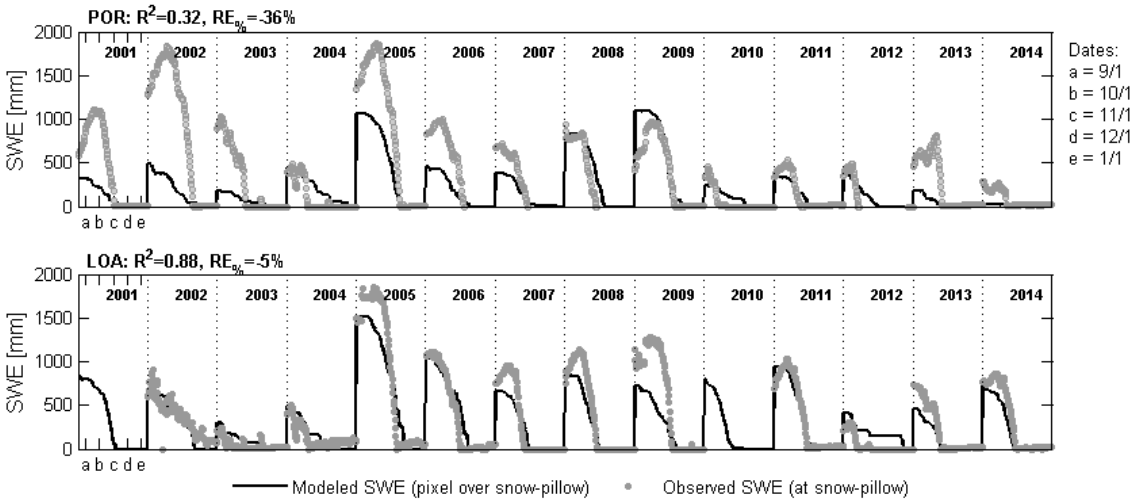

Figure S8 shows spatial modeled SWE spatial average (2001 – 2014) for 1 Sep, 1 Oct, 1 Nov, 1 Dec and 1 Jan. From September to October, SWE depth is reduced, keeping an almost invariant snow line from C2 – C5 and southern units. For C1 and C4, the snow line experiments a notorious ablation to higher elevation areas. Starting in October, SWE depth and snow line vary abruptly. At regional scale, most of the SWE depletion process is observed from September to November in C1 and C4 (northern zones). Units C2, C5 and C6 shows a delayed SWE depletion, which stabilizes in January. Units C3, C7 and C8 show an intermediate behavior between the northern and central zones possibly due to the elevation decrease of the Andes cordillera south of 35 ° S. Some differences in the SWE spatial pattern are notorious in both sides of the continental divide: the eastern side experiments slightly faster SWE depletion than the western side, process that is clearly evident in southern (C3, C7, C8) and central (C2, C5, C6) clusters.

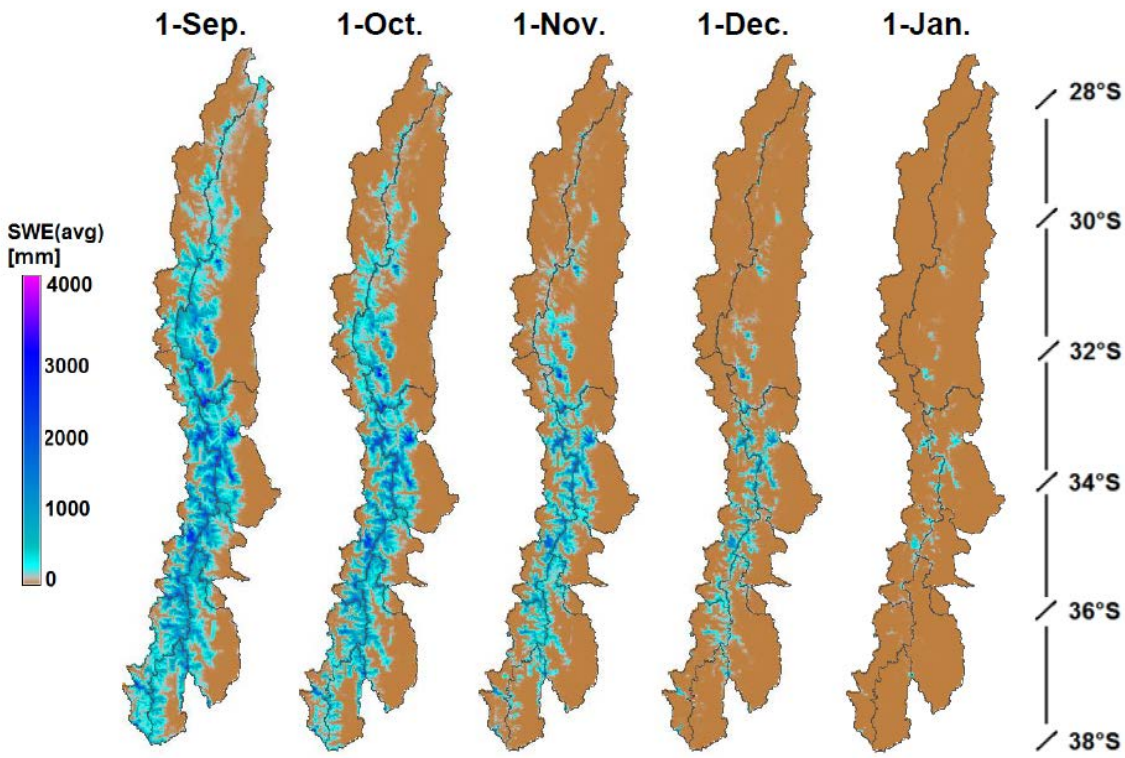

Figure S8. Evolution of SWE depletion (spatial pattern) – 2001 – 2014 average.

Bibliography

Colombi, A., De Michele, C., Pepe, M. and Rampini, A.: Estimation of daily mean air temperature from MODIS LST in Alpine areas, EARSeL EProceedings, 6(1), 38–46, 2007.

Gafurov, A., Bárdossy, A., 2009. Cloud removal methodology from MODIS snow cover product. Hydrol. Earth Syst. Sci. 13, 1361–1373.

Masiokas, M.H., Villalba, R., Luckman, B.H., Le Quesne, C., Aravena, J.C., 2006. Snowpack variations in the central Andes of Argentina and Chile, 1951-2005: Large-scale atmospheric influences and implications for water resources in the region. J. Clim. 19, 6334–6352.

Rubio-Álvarez, E. and McPhee, J.: Patterns of spatial and temporal variability in streamflow records in south central Chile in the period 1952–2003, Water Resour. Res., 46(5), W05514, doi:10.1029/2009WR007982, 2010.

Sawicz, K., Wagener, T., Sivapalan, M., Troch, P. A., and Carrillo, G.: Catchment classification: empirical analysis of hydrologic similarity based on catchment function in the eastern USA, Hydrol. Earth Syst. Sci., 15, 2895-2911, doi:10.5194/hess-15-2895-2011, 2011.

Wilks, D. S. (2005), Statistical Methods in the Atmospheric Sciences,648 pp., Elsevier, New York.